



Construction of heterojunction photoelectrode via atomic layer deposition of Fe_2O_3 on Bi_2WO_6 for highly efficient photoelectrochemical sensing and degradation of tetracycline

Sangeeta Adhikari, Seenivasan Selvaraj, Do-Heyoung Kim*

School of Chemical Engineering, Chonnam National University, Gwangju, 61186, Republic of Korea



ARTICLE INFO

Keywords:
 Heterojunction photoelectrode
 Atomic layer deposition
 $\text{Fe}_2\text{O}_3\text{-Bi}_2\text{WO}_6$
 Photoelectrochemical
 Sensing

ABSTRACT

The present paper describes the fabrication of a heterojunction photoelectrode by combining the wet chemical synthesis of Bi_2WO_6 with the formation of Fe_2O_3 layer by atomic layer deposition (ALD) technique. Fe_2O_3 with different atomic thicknesses was layered onto spin-coated Bi_2WO_6 nanoflakes by controlling the number of deposition cycles. The influence of the thickness of the Fe_2O_3 layers on photoelectrocatalytic detection and remediation was also studied. The deposition of a 15-nm layer of Fe_2O_3 on Bi_2WO_6 led to the best photoelectrochemical response under visible light activation. The performance of 15-nm $\text{Fe}_2\text{O}_3\text{-Bi}_2\text{WO}_6$ ($4.3 \mu\text{A}/\text{cm}^2$) was 3.6 times higher than that of pristine Bi_2WO_6 ($1.2 \mu\text{A}/\text{cm}^2$) at an external bias of 0.6 V. The enhanced performance was due to the increased spectral breadth of light absorption and efficient transfer of photogenerated charge carriers by the suppression of electron–hole pairs. The optimized photoelectrode detected tetracycline antibiotic in aqueous solution with a $0.3 \mu\text{M}$ limit of detection and photoelectrocatalytically degraded around 95% tetracycline. The heterojunction photoelectrode structure prepared using ALD enables inexpensive, non-enzymatic, amperometric determination and degradation of tetracycline in a stable and reproducible manner via a deduced mechanism. Our strategy can be used to fabricate photoelectrodes for a wide range of applications.

1. Introduction

Tetracyclines (TCs) belong to a group of antibiotics that are used to treat infections in aquaculture, animals, and humans [1–3]. TCs are frequently found in environmental matrices due to excretion and improper disposal. TCs exhibit high structural stability and resistance towards degradation under biological conditions and the mere presence of such antibiotics can provoke allergies in humans [4–6]. The prolonged presence of these antibiotics in the environment creates resistance, which poses a threat to ecological systems [7,8]. Thus, identification and remediation of these environmental contaminants are important. Traditional detection techniques such as microbial [9], spectroscopic [10], and chromatographic [11] measurements are either time-consuming or non-specific, and tend to be expensive because of the need for sample pretreatment [12]. In this context, a new technique that uses simpler instrumentation is required for the prompt detection of these contaminants. Photoelectrochemical sensing of environmental contaminants has attracted attention since past decades due to several versatile advantages such as fast response, ease of operation, low power consumption, and high sensitivity and selectivity [13–15]. This

technique has been efficiently utilized in the detection of immunoassays, heavy metals, antibiotics and other environmentally harmful pollutants [13,15,16]. It is a dynamic process in which a photocurrent signal is generated upon visible light absorption under application of an external bias. Although, researchers are focusing on the process of selective detection without functionalization to increase the sensitivity, but photoelectrochemical aptamer based targeted sensing is well reported [17,18].

Remediation of environmental pollutants holds equal importance in comparison to the analytical detection. Visible light active photoelectrochemical process is another emerging process which has been widely exploited for the active degradation of the various organic and inorganic pollutants with the application of small bias [19]. This process enhances the separation of electron–hole pairs by transferring the photogenerated electrons through the external circuit generating more hydroxyl radicals thereby increasing the degradation efficiency [20]. Furthermore, the amount of photons absorption to generate the photogenerated charge carriers depends on the semiconducting photoactive material that influences the separation and transfer with lowest optimum voltage.

* Corresponding author.

E-mail address: kdhh@chonnam.ac.kr (D.-H. Kim).

Amid the popular hub of visible light semiconducting materials, bismuth-based ternary oxides exhibits excellent electrochemical and optical properties [21,22]. Amongst them, bismuth tungstate (Bi_2WO_6) is an Aurivillius-phase compound which is non-toxic, efficient, and a stable semiconductor with a narrow band gap of 2.6–2.8 eV [23]. Unlike most of the semiconductor materials, Bi_2WO_6 also suffers charge recombination of photogenerated electrons and holes often limiting its overall efficiency [24]. Thus, surface modifications to Bi_2WO_6 is carried out with approaches such as incorporation of dopant [25,26], fabrication of a composite or heterojunction with another semiconductor [27–29], or alteration of morphology [30]. Morphological tuning is a principal means of controlling material properties [31]. Methods such as hydrothermal or solvothermal have been often used to produce different Bi_2WO_6 morphologies such as nanosheets [32], nanoflakes [33], nanocages [34], and self-assembled hierarchical microstructures [35,36]. Even the most fascinating morphologies of Bi_2WO_6 is not able to prevent the recombination of charge carriers. Therefore, the surface is further modified by conjoining another semiconducting material having favorable band positions with Bi_2WO_6 to promote the charge separation.

$\alpha\text{-Fe}_2\text{O}_3$ is a well-recognized visible light active semiconductor (band gap ~ 2.2 eV) and has been effectively combined with various other semiconducting materials [37]. The combination of $\text{Bi}_2\text{WO}_6\text{-Fe}_2\text{O}_3$ is quite favourable that can promote the separation of charge carriers, as $\alpha\text{-Fe}_2\text{O}_3$ has high conduction band potential than that of Bi_2WO_6 . Recently, one-dimensional heterostructured electro-spun $\text{Fe}_2\text{O}_3/\text{Bi}_2\text{WO}_6$ nanofibers were found to impede charge recombination, which results in high photocatalytic efficiency of methylene blue dye under visible light irradiation [38]. In another study, mechanically mixed $\alpha\text{-Fe}_2\text{O}_3/\text{Bi}_2\text{WO}_6$ was applied to the photocatalytic degradation of methyl orange and phenol [39]. A two-step hydrothermal–calcination procedure was also reported to develop a composite $\text{Bi}_2\text{WO}_6/\alpha\text{-Fe}_2\text{O}_3$ catalyst for photocatalytic degradation of gaseous benzene [40].

Another factor that governs the separation efficiency is the point of contact/interface between the semiconductors. Designing the heterojunction photoelectrodes can be a promising solution in charge separation through strong interfacial contact between the semiconducting materials. These structures can selectively isolate the charge carriers across the heterojunction interface and effectively separate electrons and holes [41–43]. However, the presence of defect states at the interface is not favorable from the standpoint of the outer protection layers [44,45]. The outer layer of heterojunction should be designed in such a way that it permits carrier transport to the surface and retards the recombination of carriers also.

For the fabrication of outer layers, atomic layer deposition (ALD) is an attractive technique as it has ability to produce pin-hole free ultra-thin films of controlled thickness covering the surface defects [46,47]. Moreover, it is capable of producing films for substrates of various geometries including particles, microspheres, and nanotubes [47–50] via sequential surface reactions. Herein, we report for the first time the construction of a heterojunction photoelectrodes where the outer layer of the photoelectrode is prepared by atomic layer deposition on a hydrothermally synthesized spin-coated Bi_2WO_6 as inner layer. The activity of the photoelectrode is influenced by the thickness of Fe_2O_3 layer. This study demonstrates the enhanced photoelectrochemical performance of the heterojunction due to the outer layer that acts as a catalytically active working layer as well as a passivation layer. The heterojunction photoelectrode design was utilized for the photoelectrochemical sensing and degradation of tetracycline. The $\text{Bi}_2\text{WO}_6/\text{Fe}_2\text{O}_3$ heterojunction electrode was systematically investigated with the goal of achieving the highest photoelectrochemical activity with the least possible amount of material.

2. Materials and methods

2.1. Synthesis of Bi_2WO_6 nanoflakes

Bi_2WO_6 nanoflakes were synthesized using a simple hydrothermal method. Solution A was prepared by dissolving a stoichiometric amount (0.33 g) of sodium tungstate dihydrate in 20 mL deionized water. After adding the prerequisite amount of polyvinylpyrrolidone, the solution was vigorously mixed to obtain a clear homogeneous liquid. Solution B was prepared by dissolving 0.97 g bismuth nitrate pentahydrate in 20 mL deionized water. Solution A was added slowly to solution B with vigorous stirring. The resulting homogeneous solution was transferred to a 60-mL Teflon beaker and sealed tightly. The beaker was placed in a Teflon-lined stainless steel autoclave maintained at 180 °C for a specific length of time. The hydrothermal duration was varied from 2 to 4 h. The precipitate was formed after hydrothermal reaction, and it was collected by filtration and washed with water and isopropanol to remove residual solvent. The precipitate was dried in a hot-air oven at 100 °C.

2.2. Fabrication of Bi_2WO_6 electrodes

Bi_2WO_6 nanoflake electrodes were fabricated using a spin-coating technique. The conducting substrate of the electrodes was a 2-cm² section of fluorine doped tin oxide (FTO) glass. FTO substrates were cleaned ultrasonically in acetone, isopropanol, and deionized water for 30 min each to free the surface of foreign particles. Cleaned substrates were dried in a hot-air oven at 80 °C. A homogeneously dispersed suspension of Bi_2WO_6 nanoflakes was prepared by adding 50 mg of synthesized Bi_2WO_6 powder to 5 mL of ethanol followed by ultrasonication for 50 min. A 100- μL volume of the suspension was spin-coated onto a clean, dry FTO plate using a MIDAS SPIN-1200D system at a speed of 1000 rpm for 30 s. The spin-coating process was repeated, and the electrode was dried overnight in a hot-air oven at 80 °C.

2.3. Atomic layer deposition of Fe_2O_3 on Bi_2WO_6 electrodes

ALD of Fe_2O_3 was carried out following the procedure as described elsewhere [49]. In the typical experimentation, single crystalline patterned (100) silica substrates were used for ALD of Fe_2O_3 . Bis(bis(trimethylsilyl)amide)iron(II) ($\text{Fe}(\text{btmsa})_2$) and hydrogen peroxide (H_2O_2) were used as sources of iron and oxygen, respectively. The pulsing and purging times in the ALD reactor were 1.5 and 20 s for the Fe precursor, respectively, and 0.4 and 60 s for H_2O_2 , respectively. The grown ALD Fe_2O_3 film thicknesses were examined using the spectroscopic ellipsometry technique (LSE Stokes ellipsometer, Gaertner Scientific, USA) equipped with low powered HeNe laser beam (632.8 nm).

However, in the present study, ALD of Fe_2O_3 was carried out on spin-coated Bi_2WO_6 on FTO substrates in consideration to the optimized condition to achieve uniform ALD film of Fe_2O_3 . Ultrathin Fe_2O_3 layers of 5-, 10-, 15-, and 20-nm thickness were prepared having an optimum average growth rate of 0.035 ± 0.005 nm/cycle. 5 nm Fe_2O_3 thin film requires about 143 ALD cycles. Atomically layered $\text{Fe}_2\text{O}_3/\text{Bi}_2\text{WO}_6/\text{FTO}$ samples were annealed at 550 °C in a muffle furnace that was heated at a rate of 5 °C/min over 4 h. The furnace was allowed to cool naturally. A schematic of the fabrication of atomically layered $\text{Fe}_2\text{O}_3\text{-Bi}_2\text{WO}_6$ electrodes is shown in Fig. 1.

2.4. Characterization

X-ray diffraction (XRD) analysis of the Bi_2WO_6 powder was carried out using a PANalytical X-ray diffractometer. XRD patterns were acquired at $2\theta = 20^\circ\text{--}80^\circ$ using $\text{Cu K}\alpha$ radiation. The crystallinity of ALD-deposited Fe_2O_3 on $\text{Fe}_2\text{O}_3\text{-Bi}_2\text{WO}_6/\text{FTO}$ electrodes was established using grazing incidence XRD (GIXRD) at a 1° incident angle over the same 2θ range. A field-emission scanning electron microscope (FESEM,

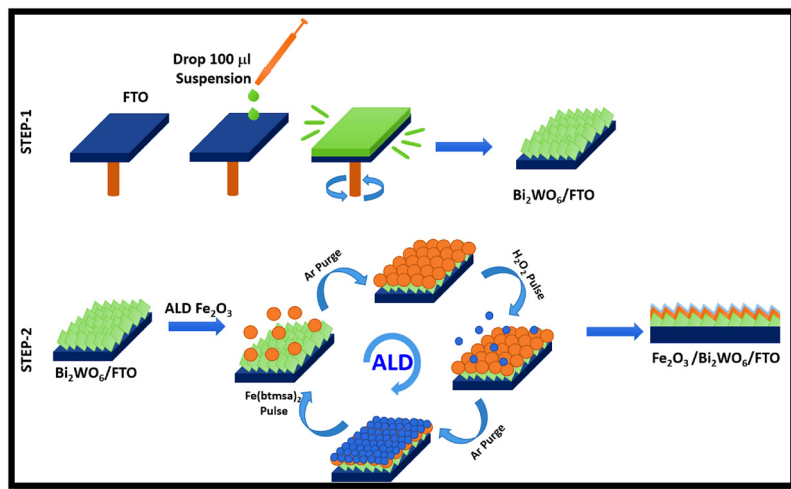


Fig. 1. Schematic illustration of Fe₂O₃-Bi₂WO₆ electrode fabrication using spin-coating (step-1) and atomic layer deposition (step-2).

JEOL JSM-7500F) coupled with an energy dispersive X-ray spectroscopic analyzer (EDS) and a transmission electron microscope (TECNAI G2 F20 TEM) were used for morphological analysis. High resolution TEM and elemental mapping images were also recorded. UV-vis diffuse reflectance spectra of fabricated electrodes were recorded with a CARY VARIAN UV-vis spectrophotometer using the FTO substrate as a reference. Photoluminescence spectra of the electrodes were obtained at an excitation wavelength of 266 nm with an Acton Research Co. Spectrograph 500i (USA) having an intensified CCD (PI-MAX3) detector. An ESCALAB-MKII X-ray spectrophotometer was used to record the spectra of optimized electrodes before and after electrochemical reaction.

2.5. Photoelectrochemical measurements

Photoelectrochemical experiments were performed with a custom-built apparatus consisting of a 150-W Xe lamp light source, an AM 1.5G filter, and an electrochemical system. The light source is procured from HS Technologies, South Korea having manufactured by Abet Technologies, USA. The spectrum of the light source imitates the ASTM standard of Air Mass 1.5G spectrum. The typical wavelength range is between 400–700 nm with the highest intense peak at 500 nm in the visible region. A monocrystalline silica reference cell was used to tune the incident intensity to 100 mW/cm². Experiments were conducted in a three-electrode quartz cell with an Ag/AgCl reference electrode and a Pt wire counter electrode. Fe₂O₃-Bi₂WO₆/FTO and Bi₂WO₆/FTO were used as working electrodes. The exposed area of the electrode was 1 cm². Photocurrents were recorded in 0.5 M Na₂SO₄ supporting electrolyte. Electrochemical impedance spectroscopy (EIS) of fabricated electrodes was performed at a signal amplitude of 10 mV in the same supporting electrolyte. Measurements were performed under room temperature conditions.

2.6. Photochemical and photoelectrochemical degradation experiments

Degradation experiments were performed using tetracycline antibiotic as a model pharmaceutical contaminant. The following experiments were conducted in batch mode with optimized bias voltage following different processes namely, photolysis and photocatalysis without applied voltage, electrolysis and electrocatalysis, and photoelectrocatalysis. A standard stock solution of the antibiotic was prepared by dissolving 20 mg tetracycline in 1000 mL deionized water. In a typical photocatalytic experiment, 30 mL of aqueous 20 mg/L tetracycline was taken in a quartz beaker, and the working electrode was inserted in the solution. The working electrode was positioned to face

the light source without application of applied bias. Photolysis was performed to exploit the effect of light on the antibiotic in the absence of working electrode and applied bias. The electrocatalytic and photoelectrocatalytic degradation studies were experimented in a three electrode cell configuration as mentioned in the previous section in the absence and presence of light, respectively using the optimized electrodes. During each experiments carried out for different processes, 1.5 ml of the solution was withdrawn from the quartz cell at regular intervals and saved for UV-vis analysis. Antibiotic degradation was determined as $[(C_0 - C)/C_0] \times 100$, where C_0 and C are the initial and final concentrations of the contaminant, respectively. Studies in the presence of scavengers were also carried out with optimized electrodes to investigate the photoelectrochemical reaction mechanism. Benzoquinone, isopropanol, and oxalic acid at 5 mM concentration were used as scavengers.

3. Results and discussion

3.1. Crystal structure analysis

The crystallinity and purity of synthesized Bi₂WO₆ indicated by XRD powder patterns as a function of hydrothermal duration are presented in Fig. 2a. Powders synthesized with a reaction time of 2 h were poorly crystalline and exhibited broad peaks at $2\theta = 20^\circ$ – 40° and 45° – 60° . However, when the hydrothermal reaction time was increased to 3 h, sharp crystalline peaks corresponding to the orthorhombic phase of Bi₂WO₆ were observed, which matched well with JCPDS Card No. 39-0256. Crystallinity increased further with increasing hydrothermal treatment as illustrated by the 4-h XRD pattern. Diffraction peaks at $2\theta = 28.43^\circ$, 32.89° , 46.99° , 55.7° , 58.67° , 68.75° , 75.96° , and 78.47° corresponded to the (113), (200), (202), (133), (262), (400), (102), and (204) reflection planes, respectively. Comparison of the 2- and 3-h patterns in the 2θ range, where the crystalline Bi₂WO₆ peaks arise, suggests that there is a poor crystalline to crystalline phase transition during this interval. A minimum reaction time of 3 h is required to obtain the crystalline phase, and the distinct morphology is achieved after 4 h. Thus, a 4-hour hydrothermal Bi₂WO₆ treatment was used for the fabrication of Bi₂WO₆/FTO electrodes and atomic layering of Fe₂O₃ on Bi₂WO₆/FTO. The XRD patterns indicate that the synthesized Bi₂WO₆ was pure and highly crystalline and did not contain other phases.

Composite XRD patterns of 5-, 10-, 15-, and 20-nm films of Fe₂O₃ ALD-deposited onto spin-coated Bi₂WO₆/FTO are presented in Fig. 2b. SnO₂ diffraction peaks from FTO are also observed and are marked as '*' in accordance with JCPDS Card No. 72-1147. Most SnO₂ and Fe₂O₃

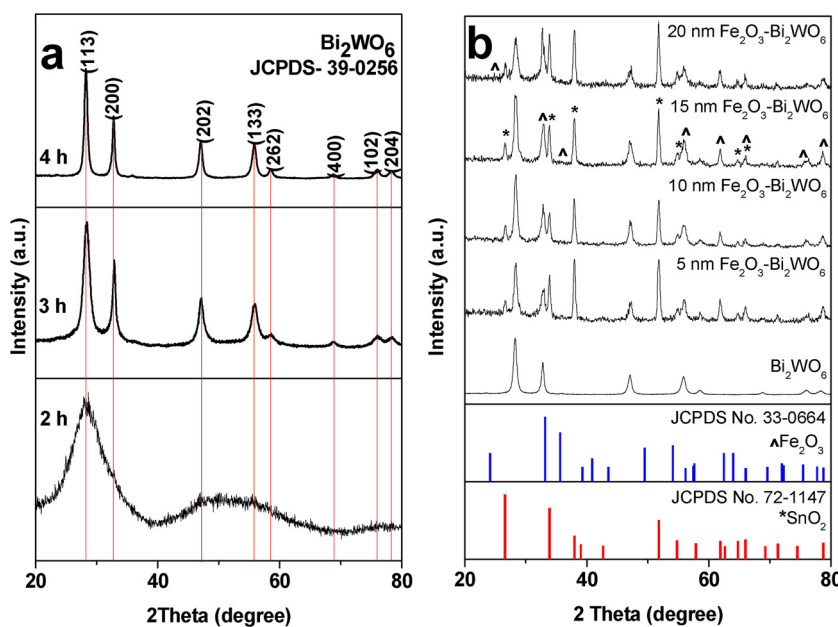


Fig. 2. (a) Composite XRD patterns of Bi_2WO_6 after different times of hydrothermal treatment; (b) XRD patterns on an FTO substrate of pristine Bi_2WO_6 and ALD-deposited 5-, 10-, 15-, and 20-nm Fe_2O_3 - Bi_2WO_6 (bars show the XRD patterns of Fe_2O_3 (') and SnO_2 (*)).

diffraction peaks overlap one another. The prominent (200) peak of Bi_2WO_6 also overlaps the 100% peak of Fe_2O_3 (marked with '^'), which corresponds to its (104) plane matching with JCPDS Card No. 33-0664. The gradual increase in intensity of the overlapped Fe_2O_3 peak relative to that of Bi_2WO_6 during deposition reflects the growth of the Fe_2O_3 layer with time. The increase in diffraction intensity is also consistent with a high conformality of the Fe_2O_3 deposit on the spin-coated Bi_2WO_6 /FTO substrate. The Fe_2O_3 produced is pure, contains no impurities, and exhibits no phase transformation. Because photoelectrochemical experiments show that 15-nm coated Fe_2O_3 - Bi_2WO_6 produces the highest photocurrent density, all SnO_2 and Fe_2O_3 components are indicated in this diffraction pattern.

3.2. Morphological analysis

FESEM images of synthesized Bi_2WO_6 illustrating its morphological development after 2, 3, and 4 h of hydrothermal treatment are shown in Fig. 3a–d. Fig. 3e and f shows topographical images of the 15-nm coated Fe_2O_3 - Bi_2WO_6 electrode. Poorly crystalline Bi_2WO_6 obtained after a reaction time of 2 h consists of small, highly agglomerated particles lacking a defined morphology (Fig. 3a). After 3 h, the random particles transform into a pseudo-spherical morphology, and some spheres appear to be largely agglomerated (Fig. 3b). However, the powder synthesized after a reaction time of 4 h shows a distinct, randomly oriented flake-like morphology (Fig. 3c). The high-resolution image (Fig. 3d) shows the flakes to be assembled as pseudo-spherical discs. The average thickness of the discs are about ~ 28 nm. The topographical image of atomically layered 15-nm Fe_2O_3 - Bi_2WO_6 is presented in Fig. 3e. It is difficult to distinguish between Bi_2WO_6 and Fe_2O_3 at low resolution. However, the high-resolution image in Fig. 3f shows the flakes to be completely coated with Fe_2O_3 . FESEM analysis did not provide an accurate estimation of film thickness. The film thickness of atomic layer deposited Fe_2O_3 was estimated by conducting bare experiments on patterned Si (100) substrates and the cross-sectional SEM micrographs were recorded as shown in Fig. S1 for 15-nm and 20-nm Fe_2O_3 films. A clear distinction between the coating and the substrate is observed confirming the thickness of the conformal films over the substrates. Thus, it could be well presumed that Bi_2WO_6 is uniformly coated with Fe_2O_3 via atomic layer deposition. Thus, high resolution transmission electron microscopy (HRTEM) was undertaken to clearly distinguish

the actual thickness.

TEM and HRTEM images of pristine Bi_2WO_6 nanoflakes synthesized after 4 h are illustrated in Fig. 4a and b, respectively. The TEM image shows that the randomly oriented small flakes assemble to form secondary flakes of greater size. The HRTEM image reveals distinct lattice fringes with calculated interplanar spacing's of 0.272 and 0.418 nm, which correspond to the (020) and (004) planes of orthorhombic Bi_2WO_6 , respectively. The elemental mapping of Bi_2WO_6 is shown in Fig. 4c. The presence solely of Bi, W, and O is consistent with the purity of synthesized Bi_2WO_6 . The TEM micrograph of an individual Bi_2WO_6 flake atomically layered with Fe_2O_3 is shown in Fig. 4d and e. The thickness and conformality of the film is consistent with the previous patterned-surface report [49]. Fig. 4d shows that the exposed surface of the Bi_2WO_6 flake is uniformly coated with ALD Fe_2O_3 having heterojunction structure. The average thickness of the Fe_2O_3 layer is ~ 14.6 nm, which approximates the intended 15-nm depth as presented in Fig. 4e. A calculated lattice spacing of 0.251 nm is assigned to the (110) plane, whereas d-spacing of 0.272 nm corresponds to the (104) plane of rhombohedral Fe_2O_3 as shown in Fig. 4f. The elemental mapping of the Fe_2O_3 -coated Bi_2WO_6 flake shows the presence of O, Fe, W, and Bi. Because Fe_2O_3 is coated on the Bi_2WO_6 , the Bi and W signals are less intense than those of Fe and O (Fig. 4g). The absence of other elemental signals indicates that the Fe_2O_3 - Bi_2WO_6 electrode is free of impurities.

3.3. Band structures and photoexcitation properties

Optical absorption plays a crucial role in photoelectrode performance. Bi_2WO_6 is known to be an active photocatalyst, whose absorption lies in the ultraviolet to visible range. Fe_2O_3 is a visible-light absorbing material. Fig. 5a displays the UV-vis absorption spectra of the fabricated electrodes comprising pristine spin-coated Bi_2WO_6 , different atomic thicknesses of Fe_2O_3 on Bi_2WO_6 , and a 15-nm Fe_2O_3 layer on FTO. A small shift in the absorption spectra of Fe_2O_3 - Bi_2WO_6 electrodes is observed with increasing Fe_2O_3 thickness. Pristine 15-nm Fe_2O_3 on FTO exhibits higher absorption than the pristine Bi_2WO_6 and Fe_2O_3 - Bi_2WO_6 electrodes. Since, the composite structure in Fe_2O_3 - Bi_2WO_6 electrode cannot represent a single band gap, thus, the band gap energies (E_g) of the pristine Bi_2WO_6 and Fe_2O_3 electrodes were calculated from their optical absorption spectra using Kubelka–Munk

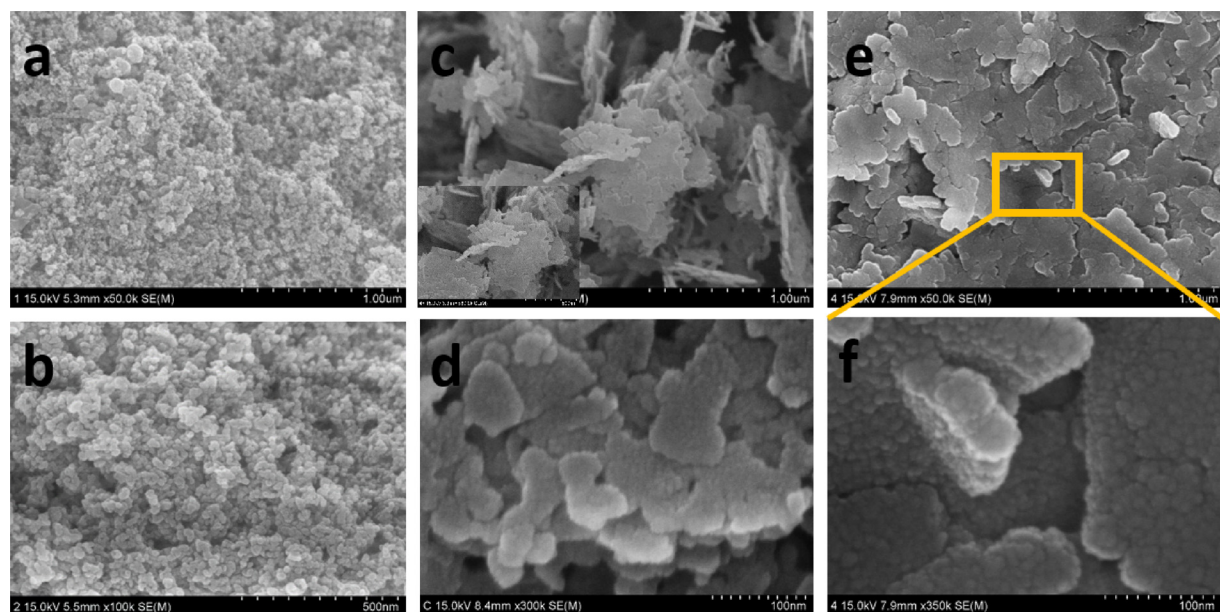


Fig. 3. FESEM images of synthesized Bi_2WO_6 powders at a reaction time of (a) 2 h, (b) 3 h, (c) 4 h (inset shows the high resolution image); (d) High resolution image at 4 h; (e) Atomic layer deposited 15-nm Fe_2O_3 on spin-coated Bi_2WO_6 ; and (f) High resolution image of 15-nm Fe_2O_3 on spin-coated Bi_2WO_6 electrode.

equation given as: $(\alpha h\nu)^{1/n} = A^*(h\nu - E_g)$, where α , h , ν , and A represents the absorption coefficient, Planck constant, vibrational frequency and a constant, respectively [51]. Tauc plot is the plot of $(\alpha h\nu)^{1/n}$ versus $h\nu$ giving the band gap through extrapolation as shown in Fig. 5b. The value of n for direct transition equals 1/2 whereas for indirect transition the value equals 2. The band gap energy values obtained from Tauc plot with indirect transition are 2.76, and 2.28 eV for pristine Bi_2WO_6 and 15-nm Fe_2O_3 on FTO, respectively. The optical results illustrate the influence of Fe_2O_3 layering on optical absorption properties, which marks an increased visible light absorption with increasing Fe_2O_3 thickness. The band positions obtained from optical analysis has been deduced and the probable reaction mechanism has been anticipated from Fig. S2.

Photoluminescence (PL) spectra of fabricated electrodes were analyzed to understand charge carriers transfer and separation during photoexcitation. The PL signal provides direct evidence of photoexcited charge recombination. The PL signals of pristine Bi_2WO_6 and Fe_2O_3 - Bi_2WO_6 electrodes with different Fe_2O_3 thicknesses are presented in Fig. 5c. All spectra exhibit a similar shape, but different peak intensities. Because the thickness of the Fe_2O_3 layers is limited by self-terminating growth during ALD, Fe_2O_3 does not create any defect states, but rather quenches the emission peaks via passivation of the Bi_2WO_6 structure [52]. Fig. 5c shows the presence of a strong emission at 400–600 nm and a weaker signal at 600–800 nm. The first emission peak arises from an interband transition from the valence band maximum to the conduction band minimum, which lies near the emission band-edge. The second peak may originate from the emission of shallow, deeply trapped states [53]. The PL intensity is greatest for pristine Bi_2WO_6 and decreases with increasing Fe_2O_3 thickness for Fe_2O_3 - Bi_2WO_6 . Thus, it can be concluded that heterojunction passivation quenches emission in the visible region. The smallest PL intensity is that of the 15-nm Fe_2O_3 - Bi_2WO_6 electrode, which suggests a high charge separation efficiency due to low recombination of photoexcited e^- - h^+ pairs. Beyond a 15-nm Fe_2O_3 thickness, visible light absorption increases, but charge carrier separation decreases due to e^- - h^+ pair recombination arising from enhanced absorption by Fe_2O_3 on the surface.

3.4. Photoelectrochemical properties

The photoelectrochemical properties of pristine Bi_2WO_6 and Fe_2O_3 - Bi_2WO_6 electrodes of varying Fe_2O_3 thicknesses were investigated by transient photocurrent measurements as a function of applied voltage. Photocurrents were measured in 0.5 M Na_2SO_4 using chopped light irradiation. All electrodes exhibit an increase in photocurrent when light is shined on the surface and a decrease to a constant value when the light is switched off (Fig. 6a). The photocurrent response increases with increasing Fe_2O_3 thickness and applied voltage. The increase in photocurrent under irradiation is consistent with enhanced electron–hole pair separation in the Fe_2O_3 - Bi_2WO_6 system. The 15-nm Fe_2O_3 - Bi_2WO_6 electrode exhibited the highest photocurrent, which suggests that this thickness produces the optimum charge separation. Beyond 15 nm, the Fe_2O_3 surface becomes more prone to recombination due to greater light absorption by Fe_2O_3 . The change in the current response under dark and in the presence of light for 15-nm Fe_2O_3 - Bi_2WO_6 electrode was plotted taking the values from Fig. 6a and presented in Fig. S3. The lowest voltage required to induce an enhanced photocurrent is 0.6 V. Because there is no significant photocurrent enhancement beyond this value, thus, 0.6 V was chosen to conduct studies of photoelectrochemical sensing and degradation. An optimum atomic layer thickness is required for greatest charge transfer efficiency. Faster charge transfer in 15-nm Fe_2O_3 - Bi_2WO_6 electrodes is supported by the EIS studies shown in Fig. 6b. EIS is a valuable tool for investigating interfacial charge transfer processes [54]. The semicircle of a Nyquist plot obtained by EIS reflects the charge transfer kinetics of the electrode in question. The smaller the diameter of the semicircle, the lower is the charge transfer resistance of the electrode [55]. All EIS spectra exhibit plots of similar shape apart from a difference in the arc of the semicircle. In Fig. 6b, the semicircle radius decreases in the order $\text{Bi}_2\text{WO}_6 > 5\text{-nm } \text{Fe}_2\text{O}_3\text{-Bi}_2\text{WO}_6 > 10\text{-nm } \text{Fe}_2\text{O}_3\text{-Bi}_2\text{WO}_6 > 20\text{-nm } \text{Fe}_2\text{O}_3\text{-Bi}_2\text{WO}_6 > 15\text{-nm } \text{Fe}_2\text{O}_3\text{-Bi}_2\text{WO}_6$. The separation efficiency and photoinduced charge transfer of e^- - h^+ pairs is optimum for the 15-nm Fe_2O_3 - Bi_2WO_6 electrode in agreement with the photoluminescence measurements. A scheme illustrating possible reactions without Fe_2O_3 and with a layer of Fe_2O_3 on Bi_2WO_6 is provided in Fig. S4.

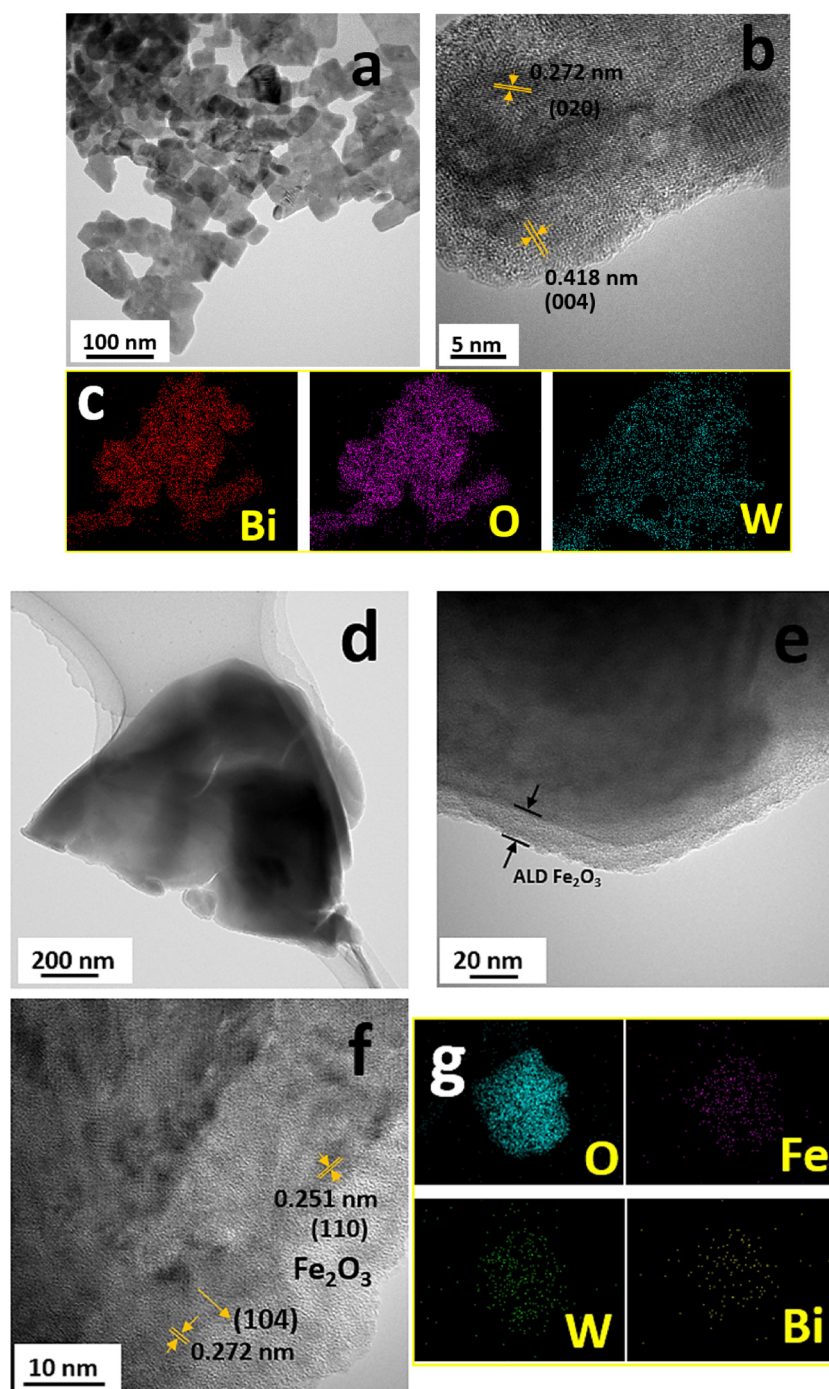


Fig. 4. (a) TEM, (b) HRTEM, and (c) elemental mapping images of pristine Bi_2WO_6 nanoflakes after 4-h synthesis; (d, e) low resolution and high resolution TEM micrographs, (f) HRTEM, and (g) elemental mapping images of a 15-nm $\text{Fe}_2\text{O}_3\text{-Bi}_2\text{WO}_6$ electrode.

3.5. Photoelectrochemical sensing

Previous photoelectrochemical experiments confirmed that the 15-nm $\text{Fe}_2\text{O}_3\text{-Bi}_2\text{WO}_6$ electrode produces the greatest photocurrent. Accordingly, the photosensitivities of pristine Bi_2WO_6 and the optimized electrode were tested for their ability to detect tetracycline (TC) in 0.5 M Na_2SO_4 at an applied bias of 0.6 V. Fig. 7a compares the photocurrent responses of Bi_2WO_6 and 15-nm $\text{Fe}_2\text{O}_3\text{-Bi}_2\text{WO}_6$ in the absence and presence of 25 μM tetracycline at 0.6 V. Addition of tetracycline to the electrolyte sharply decreases the photocurrent, which indicates that the electrodes are sensitive to the presence of the antibiotic. The photocurrent is reduced in both cases, but greater sensitivity

is achieved with the 15-nm $\text{Fe}_2\text{O}_3\text{-Bi}_2\text{WO}_6$ electrode. Fig. 7b illustrates the photoelectrochemical stability of the 15-nm $\text{Fe}_2\text{O}_3\text{-Bi}_2\text{WO}_6$ electrode in 0.5 M Na_2SO_4 in the absence of TC. The photocurrent response was recorded every 25 s under chopped visible irradiation at an applied voltage of 0.6 V for 8 cycles. The consistent rise and fall in photocurrent upon cycling occurs without significant deviation and demonstrates the repeatability of the photocurrent response. This illustrates the usefulness of the 15-nm $\text{Fe}_2\text{O}_3\text{-Bi}_2\text{WO}_6$ electrode as a photoelectrochemical sensor.

Photocurrent response was next recorded at different tetracycline concentrations (0, 0.01, 0.02, 0.03, 0.04, 0.05, 0.1, 0.25, 0.5, 1, 2.5, 5, 10, 25 μM) in 0.5 M Na_2SO_4 as shown in Fig. 7c. Successive addition of

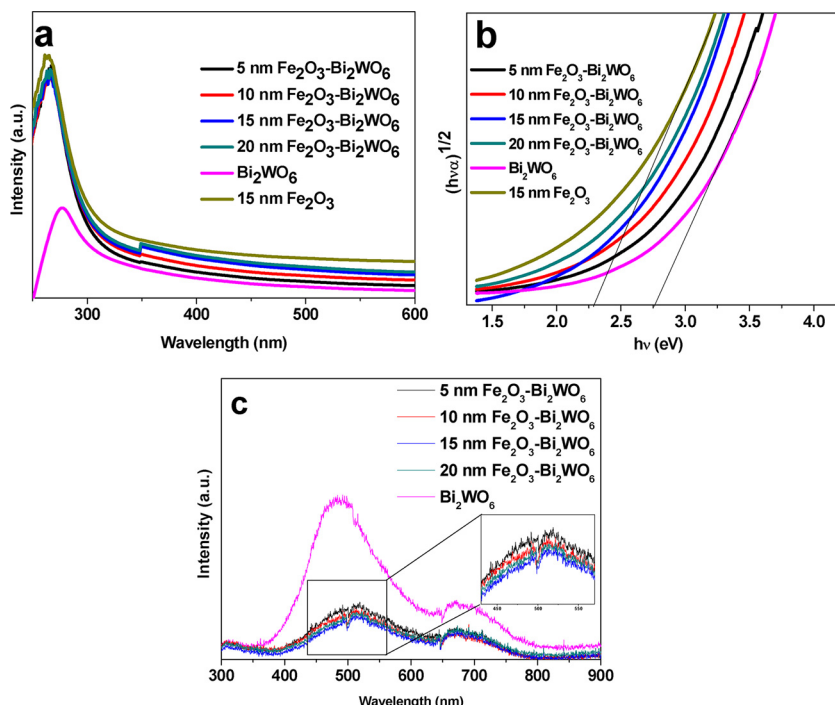


Fig. 5. (a) UV–vis absorption spectra; (b) Tauc plot from the absorption spectra; and (c) Photoluminescence spectra of pristine Bi_2WO_6 and atomically layered $\text{Fe}_2\text{O}_3\text{-Bi}_2\text{WO}_6$ photoelectrodes (a zoomed view of the spectral feature near 500 nm).

tetracycline to the electrolyte produced a continual decrease in photocurrent intensity. This performance attests to the oxidative capability of the electrode due to fast charge transfer kinetics and effective separation of electron–hole charge carriers. The change in photocurrent is expressed as $(I_o - I)/I_o$, where I_o and I are the photocurrent density in the absence and presence of tetracycline. A plot of $(I_o - I)/I_o$ versus tetracycline concentration is presented in Fig. 7d. The inset shows the linear relationship between the change in photocurrent density and the logarithm of tetracycline concentration. Linear regression of the change in photocurrent density as a function of TC concentration from 0.01 to 25 μM yields the equation $(I_o - I)/I_o = 0.2264 + 0.1202 \log(C)$, where C is the concentration of tetracycline. The linear regression coefficient is close to $R^2 = 0.99$. The calculated low limit of detection is 0.3 μM , at a signal-to-noise ratio of 3.3. The calculated lowest limit of quantitation (limit of quantitation is given by: $10 \times (\text{standard deviation of regression/slope})$) is about 1 μM which is higher than the limit of detection. This suggest that although the photocurrent response reduces linearly with addition of concentration until 0.5 μM , but reliable detection with high precision could be made with addition of 1 μM tetracycline concentration in the supporting electrolyte with applied bias of 0.6 V as the standard deviation of linear regression is 0.01 μM . Similar phenomena was observed in the studies reported by Wu et al.

[56]. The photoelectrochemical sensor exhibits a wide linear range, a low limit of detection, and an improved sensitivity due to rapid oxidation of tetracycline in the presence of photogenerated charge carriers. The process of electron transfer through the external circuit is hindered by the presence of the antibiotic, because the photogenerated charge carriers are used to oxidize tetracycline, which reduces the photocurrent density [57,58].

The specificity in the detection is another crucial factor. The photocurrent response studies were conducted with 15-nm $\text{Fe}_2\text{O}_3\text{-Bi}_2\text{WO}_6$ electrode in 0.5 M Na_2SO_4 in the presence of various other analytes such as antibiotics (ofloxacin and levofloxacin), and organic pollutants (methylene blue, rhodamine b, and congo red). The concentration of additive analytes were 50 μM , which is 2-fold greater than that of TC concentration (25 μM). The relative response of the fabricated sensor was recorded and plotted as shown in Fig. S5. The relative response of the electrode in the presence of other analytes was retained upto 90% with double the concentration of analytes present in the solution. This depicts that the fabricated electrode is fairly sensitive towards the analyte. Thus, it could be believed that further modification to the electrode can also possibly show enhanced sensitivity and selectivity.

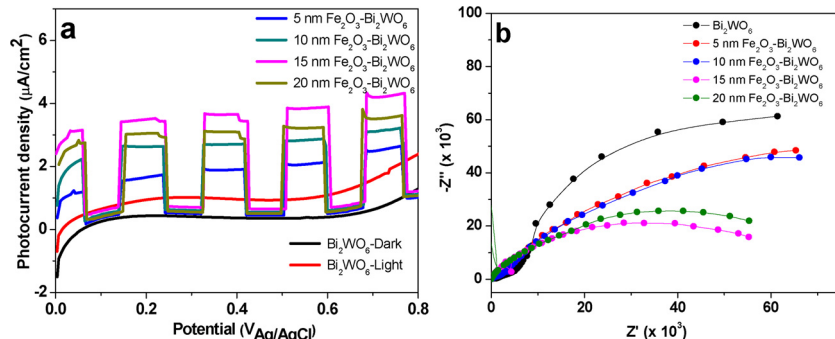


Fig. 6. (a) Transient photocurrent responses; and (b) EIS spectra of spin-coated Bi_2WO_6 and $\text{Fe}_2\text{O}_3\text{-Bi}_2\text{WO}_6$ electrodes with different Fe_2O_3 thicknesses.

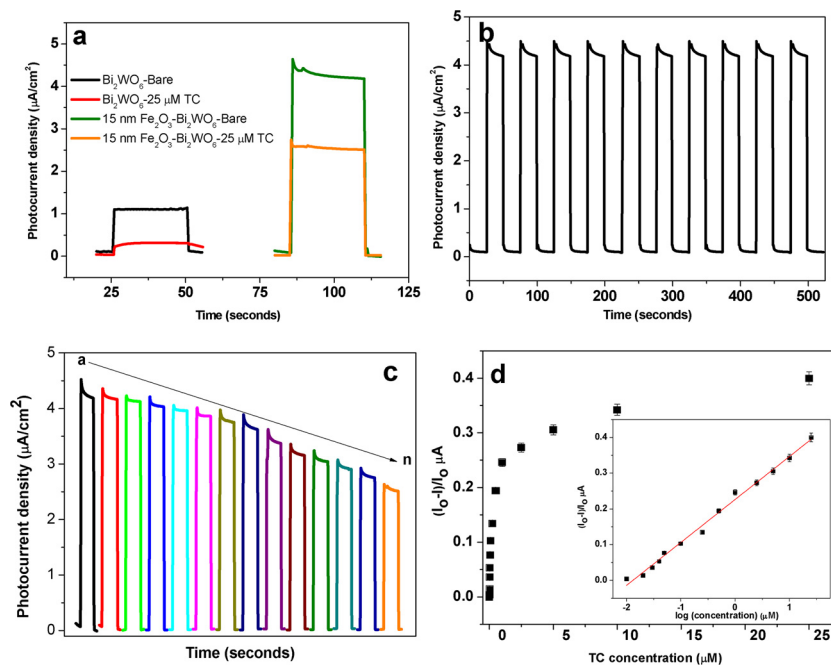


Fig. 7. (a) Comparative photocurrent responses of pristine Bi_2WO_6 and 15-nm $\text{Fe}_2\text{O}_3\text{-Bi}_2\text{WO}_6$ electrodes in the absence and presence of 25 μM TC at 0.6 V; (b) Photocurrent response stability of 15-nm $\text{Fe}_2\text{O}_3\text{-Bi}_2\text{WO}_6$ at 0.6 V; (c) Photocurrent response at increasing TC concentrations (0, 0.01, 0.02, 0.03, 0.04, 0.05, 0.1, 0.25, 0.5, 1, 2.5, 5, 10, 25 μM corresponding to a through n, respectively) using a 15-nm $\text{Fe}_2\text{O}_3\text{-Bi}_2\text{WO}_6$ electrode; and (d) Linear calibration curve for the detection of TC. All the experiments were conducted in 0.5 M Na_2SO_4 .

3.6. Photochemical and photoelectrochemical degradation

Although, the photocurrent responses of the fabricated photoelectrodes present the superiority of 15-nm $\text{Fe}_2\text{O}_3\text{-Bi}_2\text{WO}_6$ in comparison to Bi_2WO_6 and other electrodes, but, the photocatalytic degradation of tetracycline in the presence of pristine Bi_2WO_6 and $\text{Fe}_2\text{O}_3\text{-Bi}_2\text{WO}_6$ electrodes of varying Fe_2O_3 thicknesses has also been carried out. Fig. 8a present the concentration profile for tetracycline degradation which clearly indicates that beyond 15-nm Fe_2O_3 thickness on Bi_2WO_6 , the degradation is suppressed probably due to additional Fe_2O_3 layers. This was further supported by the plot of first order rate constants of all the electrodes (Fig. 8b), where the highest rate of degradation $8.06 \times 10^{-3} \text{ min}^{-1}$ was observed for 15-nm $\text{Fe}_2\text{O}_3\text{-Bi}_2\text{WO}_6$, which is approximately 1.5 times higher and lower than pristine Bi_2WO_6 and 20-nm $\text{Fe}_2\text{O}_3\text{-Bi}_2\text{WO}_6$ photoelectrodes. To further enhance the catalytic degradation, applied bias of 0.6 V was applied and a comparative degradation studies between Bi_2WO_6 and $\text{Fe}_2\text{O}_3\text{-Bi}_2\text{WO}_6$ electrodes were conducted for various catalytic processes as discussed below.

Catalytic degradation of tetracycline was carried out using Bi_2WO_6 and 15-nm $\text{Fe}_2\text{O}_3\text{-Bi}_2\text{WO}_6$ electrodes at an applied bias of 0.6 V. Catalytic oxidation of tetracycline was conducted using various electrochemical, photochemical, and photoelectrochemical processes. The concentration versus time profiles for different processes are presented in Fig. 8c and d. Photoelectrochemical degradation of a contaminant depends on its concentration and is influenced by the presence of a supporting electrolyte, which increases the mobility of ions in solution. However, all experiments were conducted without a supporting electrolyte. The catalytic degradation of tetracycline solely under visible light (photolysis, PL) was carried out to understand the influence of light on the antibiotic in the absence of electrodes. Electrolysis (EL) of tetracycline on a bare FTO substrate was undertaken to understand the influence of an applied voltage on the catalytic process. The fabricated electrodes are not used during these experiments. Both the processes are independent of the materials. Tetracycline degradation by either PL or EL was approximately 25%. A 10% difference was observed between the electrocatalytic (EC) degradations (in the presence of a photoelectrode without irradiation) conducted at 15-nm $\text{Fe}_2\text{O}_3\text{-Bi}_2\text{WO}_6$ (41%) and Bi_2WO_6 (31%) photoelectrodes. The photocatalytic (PC) and photoelectrocatalytic (PEC) processes showed greatly enhanced degradation with the 15-nm $\text{Fe}_2\text{O}_3\text{-Bi}_2\text{WO}_6$ photoelectrodes. TC degradation

reached 95% within 90 min when visible irradiation and an applied bias of 0.6 V was employed on 15-nm $\text{Fe}_2\text{O}_3\text{-Bi}_2\text{WO}_6$. Compared with Bi_2WO_6 photoelectrodes (59% degradation), Fe_2O_3 atomic layering significantly enhanced the PEC degradation of tetracycline.

Shukla et al. [59] have proposed a general kinetic scheme, whereby network modeling is performed taking all catalytic processes into consideration. The final rate expression can be written using the following equation:

$$A(C_0 - C) + \ln\left(\frac{C_0}{C}\right) = Bt \quad (1)$$

Here, A and B are model fitting constants, and C_0 and C are the initial and final dye concentration at time, t. The model fitting parameters are quite sensitive to the applied bias. The value of A is indicative of the rate of the catalytic degradation. A significantly greater value of the A represents the reduced rate of degradation and the reaction is independent of the zero order kinetics. The application of bias hinders the charge carrier recombination and promotes the reaction. The model constant B is dependent on the value of A and is not trend dependent. The red solid lines in Fig. 8c and d represent the fitting of the concentration points to the model. To further understand the effect of applied bias on the model parameters (A and B), experiments with varying voltages 1 V and 1.2 V using 15-nm $\text{Fe}_2\text{O}_3\text{-Bi}_2\text{WO}_6$ electrode has been carried out and the respective concentration profiles has been presented in Fig. S6. The corresponding degradation percentage and parameter values has been tabulated in Table S1. The value of parameter A reduces with increasing voltage suggesting the increased rate of reaction and increment in degradation efficiency.

The percentage degradation of tetracycline, model fitting parameters, and first-order kinetic parameters are collected in Table 1. The data points from the concentration profile follow linear first-order kinetics until 60 min. Thus, first-order rate constants ($k, \text{ min}^{-1}$) and regression coefficients (R^2) are reported for all catalytic processes from $t = 0$ to 60 min. Kinetic plots of $\ln(C/C_0)$ versus time for Bi_2WO_6 and 15-nm $\text{Fe}_2\text{O}_3\text{-Bi}_2\text{WO}_6$ photoelectrodes are presented in Fig. 8e and f, respectively. Fitting parameters and rate constants are reported in Table 1. The results show that the rate of PEC degradation is greater with 15-nm $\text{Fe}_2\text{O}_3\text{-Bi}_2\text{WO}_6$ photoelectrodes ($24.69 \times 10^{-3} \text{ min}^{-1}$) than with pristine Bi_2WO_6 photoelectrodes ($9.81 \times 10^{-3} \text{ min}^{-1}$). Moreover, the photoelectrocatalytic degradation rate with 15-nm $\text{Fe}_2\text{O}_3\text{-Bi}_2\text{WO}_6$ is

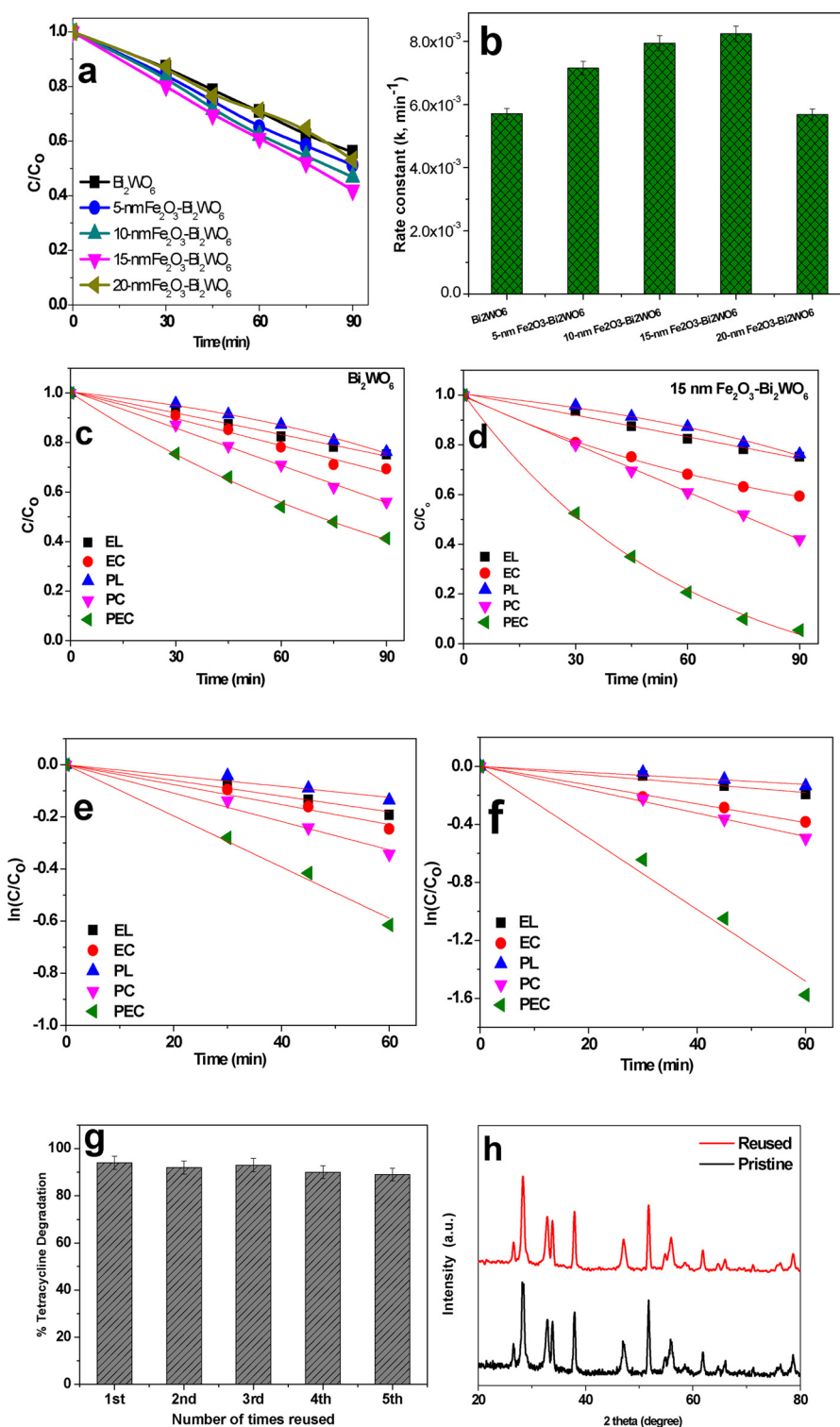


Fig. 8. Concentration profile and first order rate constants (a, b) of Bi_2WO_6 and $\text{Fe}_2\text{O}_3\text{-Bi}_2\text{WO}_6$ electrodes with different Fe_2O_3 thicknesses; Concentration-time profiles (c, d); and first-order kinetic plots (e, f) for various tetracycline degradation techniques (EL = electrolysis, EC = electrocatalysis, PL = photolysis, PC = photocatalysis, and PEC = photoelectrocatalysis) using Bi_2WO_6 and $15\text{-nm Fe}_2\text{O}_3\text{-Bi}_2\text{WO}_6$ electrodes; (g) Photoelectrocatalytic stability tests of $\text{Fe}_2\text{O}_3\text{-Bi}_2\text{WO}_6$ electrodes; and (h) XRD patterns of a $15\text{-nm Fe}_2\text{O}_3\text{-Bi}_2\text{WO}_6$ photoelectrode before and after five experiments.

3 times higher than the rate of the photocatalytic process ($8.06 \times 10^{-3} \text{ min}^{-1}$). The regression coefficients for all catalytic processes are greater than 0.98. The above results are consistent with the process of charge-transfer enhancement under an applied bias of 0.6 V in the presence of visible light, which provides the driving force for electron transfer from the CB of Fe_2O_3 to the CB of Bi_2WO_6 . The

effective separation of electron–hole pairs contributes to the enhanced catalytic efficiency.

Stability is crucial in practical applications. Thus, this property of $15\text{-nm Fe}_2\text{O}_3\text{-Bi}_2\text{WO}_6$ photoelectrodes was tested by carrying out the catalytic degradation of tetracycline for 5 five consecutive cycles as shown in Fig. 8g. Prior to PEC degradation studies, the same electrode

Table 1

Percentage degradation, model fitting parameters, and first-order kinetic parameters for tetracycline degradation with Bi_2WO_6 and 15-nm $\text{Fe}_2\text{O}_3/\text{Bi}_2\text{WO}_6$ photoelectrodes.

Process	Percentage degradation (%)	Model fitted parameters ($\times 10^{-2} \text{ min}^{-1}$)		First-order parameters	
		A	B	k ($\times 10^{-3} \text{ min}^{-1}$)	R^2
Bi_2WO_6	EL	25	6.4	0.67	3.01
	EC	31	6.8	0.99	3.82
	PL	24	7.1	0.61	2.08
	PC	44	7.8	1.23	5.44
	PEC	59	8.0	1.72	9.81
	EC	41	7.6	1.39	6.48
15-nm $\text{Fe}_2\text{O}_3/\text{Bi}_2\text{WO}_6$	PC	58	8.8	2.04	8.06
	PEC	95	6.1	4.34	24.69

was used for PEC sensing of tetracycline to understand its stability in this context. After the sensing experiment, the photoelectrode was washed with water and isopropanol followed by drying overnight in a hot-air oven at 100 °C. The same process was followed after each reuse of the electrode in the consecutive PEC experiment, which produced no significant difference in performance from the first to the fifth use. The stability of the photoelectrode is attributed to the Fe_2O_3 coating, which acts as a protective layer in addition to its role as an active heterojunction material. Composite XRD patterns of a pristine 15-nm Fe_2O_3 - Bi_2WO_6 photoelectrode before its first and after its fifth use are shown in Fig. 8h. The pristine and reused samples do not show any apparent change in crystal structure as a consequence of photoelectrochemical reaction, and no new peaks appear following the multiple catalytic cycles. Nevertheless, a detailed XPS study of a photoelectrode before and after a PEC reaction was also conducted.

The composition and chemical states of the electrode before and after photoelectrochemical sensing and five consecutive degradation experiments were examined using X-ray photoelectron spectroscopy. Detailed Bi-4f, W-4f, Fe-2p, and O-1s XPS spectra before and after these experiments are shown in Fig. 9. In Fig. 9a, Bi-4f spectra of the pristine and reused electrode are deconvoluted into four peaks. The major peaks at 159.4 eV and 164.78 eV correspond to the $\text{Bi}-4\text{f}_{7/2}$ and $\text{Bi}-4\text{f}_{5/2}$ transitions, respectively, of the Bi^{3+} sites in both electrodes [60]. The less intense peaks at 157.3 and 162.6 eV are attributed to weak $\text{Bi}-4\text{f}_{7/2}$ and $\text{Bi}-4\text{f}_{5/2}$ spin-orbit doublets, respectively, suggesting that some bismuth in the nanoflakes exists in the (+3-x) valence state as a sub-stoichiometric phase [61]. The lower oxidation state is due to the presence of oxygen vacancies in the structure [62]. No significant change in structure is observed after the cycling tests. The W-4f spectra in Fig. 9b show peaks at 35.9 and 38.06 eV, which are assigned to $\text{W}-4\text{f}_{7/2}$ and $\text{W}-4\text{f}_{5/2}$ transitions, respectively, and indicate the presence of the W^{6+} oxidation state [63]. The binding energies shift to slightly lower values in the reused electrode. In Fig. 9c, binding energies at 716.3 and 710.9 eV correspond to the $\text{Fe}-2\text{p}_{1/2}$ and $\text{Fe}-2\text{p}_{3/2}$ transitions, respectively, and indicate the presence of Fe^{3+} in the structure [64]. The shoulder or satellite peaks at 712.7, 709.6, and 720.01 eV are typical of Fe_2O_3 [65]. The O-1s spectra in Fig. 9d contain intense peaks at 532.5 and 530.9 eV in both electrodes that are assigned to oxygen present in the lattice and in bridging hydroxyl groups [25]. The decrease in intensity is related to the number of oxygen atoms present at the electrode surface [66]. The above results show that the fabricated photoelectrode is structurally stable throughout its photoelectrochemical reactions.

3.7. Photoelectrochemical mechanism

The above results describe the outstanding performance of the 15-nm Fe_2O_3 - Bi_2WO_6 photoelectrodes. Investigation of the photoelectrocatalytic mechanism involved was pursued by performing catalytic

experiments in the presence of scavengers to identify the oxidative radical species that contributed toward tetracycline degradation for both Bi_2WO_6 and 15-nm Fe_2O_3 - Bi_2WO_6 photoelectrodes. The duration of the experiments was 60 min, and TC degradation in the absence of scavengers was used as a control. Benzoquinone (BQ), isopropyl alcohol (IPA), and oxalic acid (OA) were used as trapping agents to capture superoxide radicals (O_2^-), hydroxyl radicals (OH^\cdot), and holes (h^\cdot), respectively [27,67]. The concentration versus time profiles of experiments performed in the presence of scavengers are displayed in Fig. 10a and c for Bi_2WO_6 and 15-nm Fe_2O_3 - Bi_2WO_6 photoelectrodes, respectively. For Bi_2WO_6 photoelectrode, there was negligible effect in the presence of superoxide radical scavenger, whereas significant inhibition of the degradation reaction was observed in the presence of the hydroxyl radical scavenger suggesting the degradation reaction with the pristine Bi_2WO_6 is due to formation of hydroxyl radicals (Fig. 10a). Partial contribution from the hole scavenger can be observed but the reaction is not hindered as significant as in the presence of isopropyl alcohol. On the other hand, with 15-nm Fe_2O_3 - Bi_2WO_6 photoelectrode, oxalic acid has the greatest effect in inhibiting tetracycline degradation, whereas the effect of IPA is intermediate and that of benzoquinone is negligible as presented in Fig. 10c. First-order kinetic plots of the data are shown in Fig. 10b and d. The kinetic plot for TC degradation in the presence of scavengers supports the above discussion. The lowest rate of degradation $3.49 \times 10^{-3} \text{ min}^{-1}$ is observed in presence of hydroxyl radical scavenger with Bi_2WO_6 photoelectrode (Fig. 10b). Hole-scavenger oxalic acid produces the most dramatic decrease in the rate of photodegradation ($8.13 \times 10^{-3} \text{ min}^{-1}$) compared with the control ($24.69 \times 10^{-3} \text{ min}^{-1}$) as observed from Fig. 10d. Tetracycline degradation is inhibited by a factor of 1.7 in presence of IPA ($13.94 \times 10^{-3} \text{ min}^{-1}$) and negligibly in the presence of BQ ($20.01 \times 10^{-3} \text{ min}^{-1}$). Consequently, photogenerated holes are the principal species contributing to the photoelectrocatalytic degradation of tetracycline, which is consistent with the prediction of the band diagram (Fig. S2) constructed from the optical analysis for Fe_2O_3 - Bi_2WO_6 heterojunction electrode.

Literature reports several catalytic studies with surface modification, composite formation and doping in Bi_2WO_6 and Fe_2O_3 structures highlighting different mechanisms [68–70]. Hierarchical Bi_2WO_6 composed of nanoflakes were synthesized and the photocatalytic degradation studies with rhodamine B as pollutant was investigated. A superior catalytic activity was observed with erythrocyte-like structure of Bi_2WO_6 with complete degradation of the pollutant within 15 min having concentration 10 mg/L in the presence of H_2O_2 as catalytic promoter [71]. A new strategy was put forward by the same group, where, PO_4 -doped Bi_2WO_6 was investigated for degradation of variant aqueous pollutants, such as rhodamine B, Cr(VI), and phenol in the presence of citric acid and H_2O_2 to ensure faster and complete degradation within 40, 60 and 200 min, respectively. The degradation studies of several antibiotics were also investigated [72]. It can be well

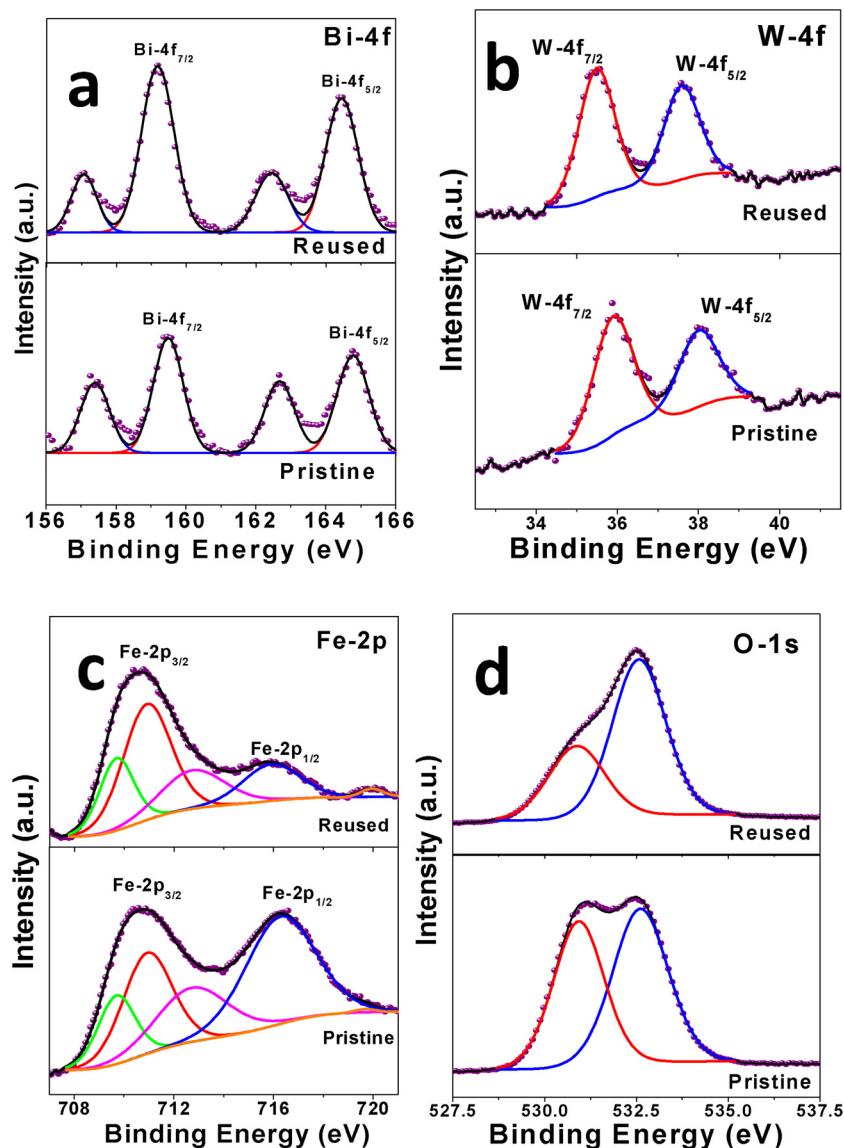


Fig. 9. XPS spectra of pristine and reused 15-nm Fe_2O_3 - Bi_2WO_6 photoelectrodes showing the deconvoluted peaks for (a) Bi-4f , (b) W-4f , (c) Fe-2p , and (d) O-1s transitions.

noted that the photocatalytic studies are dependent on factors such as concentration of pollutant, catalyst, applied bias and also addition of promoters. The present studies still stands out as near to complete degradation occurs with low applied voltage without addition of influential promoters.

In summary, the experimentally established PEC mechanism explains the photoelectrochemical sensitivity and tetracycline degradation capability of the photoelectrodes. The Bi_2WO_6 nanoflakes increase light absorption due to their two-dimensional interconnected structure, and the photoactive 15-nm Fe_2O_3 layer on the Bi_2WO_6 inner layer also acts as a protective casing. The Bi_2WO_6 and Fe_2O_3 band positions favor formation of heterojunction that enhances charge separation. Upon illumination of the photoelectrode, both Bi_2WO_6 and Fe_2O_3 become excited leading to transfer of an electron from the valence band to the conduction band and creation of a hole in the valence band. Because the conduction and valence bands of Fe_2O_3 lie above those of Bi_2WO_6 , the photogenerated electron in the CB of Fe_2O_3 readily flows into the CB of Bi_2WO_6 . The photogenerated holes are transferred from the VB of Bi_2WO_6 to that of Fe_2O_3 . Thus, charge carrier recombination is suppressed as confirmed by PL spectroscopy and photoelectrochemical studies. The photogenerated holes that accumulate in the VB of Fe_2O_3

participate in tetracycline oxidation, and the photogenerated electrons flow through the external circuit under an applied bias. The design of the heterojunction photoelectrode using atomic layer deposition significantly enhances the charge transfer kinetics and overall performance efficiency. The experimental setup of the photoelectrocatalytic process and the accompanying reaction mechanism are shown schematically in Fig. 10.

4. Conclusions

A novel ALD Fe_2O_3 - Bi_2WO_6 heterojunction structure was constructed and used as a photoelectrode to detect and oxidize tetracycline. A 15-nm thick Fe_2O_3 layer on spin-coated Bi_2WO_6 triggers visible light absorption and electron transfer to the conduction band of Bi_2WO_6 , which results in rapid separation of photogenerated electron–hole pairs. The photoelectrochemical device detects tetracycline rapidly over a long linear concentration range with a low limit of detection. The 15-nm Fe_2O_3 - Bi_2WO_6 electrode shows enhanced photoelectrocatalytic activity toward tetracycline oxidation, in which the Fe_2O_3 layer acts concomitantly as a casing, light absorber, and protector of the photoelectrode. The present results demonstrate the success of atomic layer

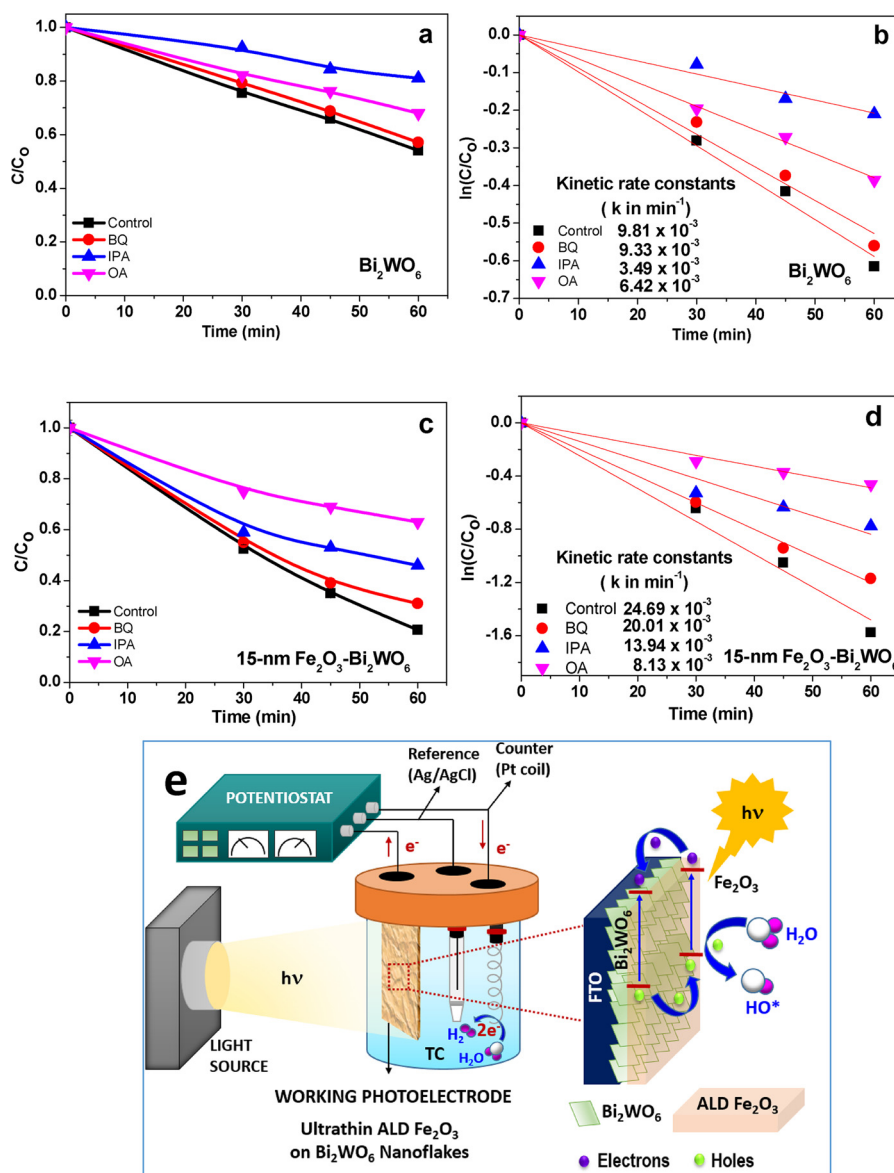


Fig. 10. (a, c) Concentration versus time profiles in the presence of scavengers (BQ, benzoquinone; IPA, isopropyl alcohol; OA, oxalic acid); (b, d) First-order kinetic plots of TC degradation by PEC with Bi_2WO_6 and 15-nm $\text{Fe}_2\text{O}_3\text{-Bi}_2\text{WO}_6$ photoelectrodes in the presence of scavengers, respectively; and (e) Schematic illustration of the experimental apparatus and the proposed photoelectrocatalytic mechanism upon visible light irradiation.

deposition in the development of a $\text{Fe}_2\text{O}_3\text{-Bi}_2\text{WO}_6$ heterojunction photoelectrode for multifunctional detection and remediation.

Acknowledgments

The authors would like to thank the National Research Foundation of Korea (NRF-2015M3A7B 4050 424) and the Korea Research Fellowship Program (KRF grant no. 2018H1D3A1A02074832) for support. We also thank the Korea Basic Science Institute (KBSI) at Gwangju center for SEM and TEM analysis.

Appendix A. Supplementary data

Supplementary material related to this article can be found, in the online version, at doi:<https://doi.org/10.1016/j.apcatb.2018.11.043>.

References

[1] C. Gu, K.G. Karthikeyan, Interaction of tetracycline with aluminum and iron

hydrous oxides, Environ. Sci. Technol. 39 (2005) 2660–2667.

[2] L. Rimoldi, D. Meroni, G. Cappelletti, S. Ardizzone, Green and low cost tetracycline degradation processes by nanometric and immobilized TiO_2 systems, Catal. Today 281 (2017) 38–44.

[3] G. Li, Y. Feng, W. Zhu, X. Zhang, Enhanced adsorptive performance of tetracycline antibiotics on lanthanum modified diatomite, Korean J. Chem. Eng. 32 (2015) 2109–2115.

[4] V. Homem, L. Santos, Degradation and removal methods of antibiotics from aqueous matrices – a review, J. Environ. Manage. 92 (2011) 2304–2347.

[5] F. Chen, Q. Yang, J. Sun, F. Yao, S. Wang, Y. Wang, X. Wang, X. Li, C. Niu, D. Wang, G. Zeng, Enhanced photocatalytic degradation of tetracycline by AgI/BiVO_4 heterojunction under visible-light irradiation: mineralization efficiency and mechanism, ACS Appl. Mater. Interfaces 8 (2016) 32887–32900.

[6] K.G. Pavithra, P. Senthil Kumar, P. Sundar Rajan, A. Saravanan, M. Naushad, Sources and impacts of pharmaceutical components in wastewater and its treatment process: a review, Korean J. Chem. Eng. 34 (2017) 2787–2805.

[7] R. Daghbir, P. Drogui, Tetracycline antibiotics in the environment: a review, Environ. Chem. Lett. 11 (2013) 209–227.

[8] Y. Zhang, J. Shi, Z. Xu, Y. Chen, D. Song, Degradation of tetracycline in a schorl/ H_2O_2 system: Proposed mechanism and intermediates, Chemosphere 202 (2018) 661–668.

[9] H.-Y. Chen, Y.-D. Liu, B. Dong, Biodegradation of tetracycline antibiotics in A/O moving-bed biofilm reactor systems, Bioprocess Biosyst. Eng. 41 (2018) 47–56.

[10] J. Zhao, P. Liu, H. Yuan, Y. Peng, Q. Hong, M. Liu, Rapid detection of tetracycline residues in duck meat using surface enhanced raman spectroscopy, J. Spectrosc.

2016 (2016) 6.

[11] A. Pena, C.M. Lino, R. Alonso, D. Barceló, Determination of tetracycline antibiotic residues in edible swine tissues by liquid chromatography with spectrofluorometric detection and confirmation by mass spectrometry, *J. Agric. Food Chem.* 55 (2007) 4973–4979.

[12] J. Wang, D. Zhi, H. Zhou, X. He, D. Zhang, Evaluating tetracycline degradation pathway and intermediate toxicity during the electrochemical oxidation over a Ti/Ti_xO_y anode, *Water Res.* 137 (2018) 324–334.

[13] Y. Zang, J. Lei, H. Ju, Principles and applications of photoelectrochemical sensing strategies based on biofunctionalized nanostructures, *Biosens. Bioelectron.* 96 (2017) 8–16.

[14] Y. Liu, X. Gan, B. Zhou, B. Xiong, J. Li, C. Dong, J. Bai, W. Cai, Photoelectrocatalytic degradation of tetracycline by highly effective TiO₂ nanopore arrays electrode, *J. Hazard. Mater.* 171 (2009) 678–683.

[15] H. Li, J. Li, Z. Yang, Q. Xu, X. Hu, A novel photoelectrochemical sensor for the organophosphorus pesticide dichlofenthion based on nanometer-sized titania coupled with a screen-printed electrode, *Anal. Chem.* 83 (2011) 5290–5295.

[16] R. Xu, D. Wei, B. Du, W. Cao, D. Fan, Y. Zhang, Q. Wei, H. Ju, A photoelectrochemical sensor for highly sensitive detection of amyloid beta based on sensitization of Mn:CdSe to Bi₂WO₆/CdS, *Biosens. Bioelectron.* 122 (2018) 37–42.

[17] I. Ibrahim, H.N. Lim, R. Mohd Zawawi, A. Ahmad Tajudin, Y.H. Ng, H. Guo, N.M. Huang, A review on visible-light induced photoelectrochemical sensors based on CdS nanoparticles, *J. Mater. Chem. B* 6 (2018) 4551–4568.

[18] D. Jin, A. Gong, H. Zhou, Visible-light-activated photoelectrochemical biosensor for the detection of the pesticide acetochlor in vegetables and fruit based on its inhibition of glucose oxidase, *RSC Adv.* 7 (2017) 17489–17496.

[19] H. Chen, Y.-P. Peng, T.-Y. Chen, K.-F. Chen, K.-L. Chang, Z. Dang, G.-N. Lu, H. He, Enhanced photoelectrochemical degradation of Ibuprofen and generation of hydrogen via BiOI-deposited TiO₂ nanotube arrays, *Sci. Total Environ.* 633 (2018) 1198–1205.

[20] V. Cristina, G. Longobucco, N. Marchetti, S. Caramori, C.A. Bignozzi, A. Martucci, A. Molinari, R. Boaretto, C. Stevanin, R. Argazzi, M. Dal Colle, R. Bertoncello, L. Pasti, Photoelectrochemical degradation of pharmaceuticals at β25 modified WO₃ interfaces, *Catal. Today* (2018), <https://doi.org/10.1016/j.cattod.2018.09.020>.

[21] L. Chen, J. He, Y. Liu, P. Chen, C.-T. Au, S.-F. Yin, Recent advances in bismuth-containing photocatalysts with heterojunctions, *Chin. J. Catal.* 37 (2016) 780–791.

[22] F. Chen, Q. Yang, Y. Wang, F. Yao, Y. Ma, X. Huang, X. Li, D. Wang, G. Zeng, H. Yu, Efficient construction of bismuth vanadate-based Z-scheme photocatalyst for simultaneous Cr(VI) reduction and ciprofloxacin oxidation under visible light: Kinetics, degradation pathways and mechanism, *Chem. Eng. J.* 348 (2018) 157–170.

[23] G. Zhang, Z. Hu, M. Sun, Y. Liu, L. Liu, H. Liu, C.-P. Huang, J. Qu, J. Li, Formation of Bi₂WO₆ bipyramids with vacancy pairs for enhanced solar-driven photoactivity, *Adv. Funct. Mater.* 25 (2015) 3726–3734.

[24] X. Meng, Z. Zhang, Synthesis, analysis, and testing of BiOBr-Bi₂WO₆ photocatalytic heterojunction semiconductors, *Int. J. Photoenergy* 2015 (2015) 12.

[25] H. Huang, K. Liu, K. Chen, Y. Zhang, Y. Zhang, S. Wang, Ce and F comodification on the crystal structure and enhanced photocatalytic activity of Bi₂WO₆ photocatalyst under visible light irradiation, *J. Phys. Chem. C* 118 (2014) 14379–14387.

[26] K. Lee, C.-H. Lee, J.Y. Cheong, S. Lee, I.-D. Kim, H.-I. Joh, D.C. Lee, Expanding depletion region via doping: Zn-doped Cu₂O buffer layer in Cu₂O photocathodes for photoelectrochemical water splitting, *Korean J. Chem. Eng.* 34 (2017) 3214–3219.

[27] S. Adhikari, D.-H. Kim, Synthesis of Bi₂S₃/Bi₂WO₆ hierarchical microstructures for enhanced visible light driven photocatalytic degradation and photoelectrochemical sensing of ofloxacin, *Chem. Eng. J.* 354 (2018) 692–705.

[28] N. Bagvand, S. Sharifnia, E. Karamian, A visible-light-active BiFeO₃/ZnS nanocomposite for photocatalytic conversion of greenhouse gases, *Korean J. Chem. Eng.* 35 (2018) 1735–1740.

[29] Z. Lin, J. Gong, P. Fu, Hierarchical Fe₂O₃/Bi₂WO₆ nanoplates with enhanced xylene sensing performance, *J. Mater. Sci. Mater. Electron.* 28 (2017) 4424–4430.

[30] J. Zhang, T. Wang, X. Chang, A. Li, J. Gong, Fabrication of porous nanoflake BiMO_x (M = W, V, and Mo) photoanodes via hydrothermal anion exchange, *Chem. Sci.* 7 (2016) 6381–6386.

[31] H. Tong, S. Ouyang, Y. Bi, N. Umezawa, M. Oshikiri, J. Ye, Nano-photocatalytic materials: possibilities and challenges, *Adv. Mater.* 24 (2012) 229–251.

[32] T. Hu, H. Li, R. Zhang, N. Du, W. Hou, Thickness-determined photocatalytic performance of bismuth tungstate nanosheets, *RSC Adv.* 6 (2016) 31744–31750.

[33] Synthesis of bismuth tungstate (Bi₂WO₆) nanoflakes and their field emission investigation, *AIP Conf. Proc.* 1731 (2016) 1–3 120029.

[34] M. Shang, W. Wang, H. Xu, New Bi₂WO₆ nanocages with high visible-light-driven photocatalytic activities prepared in refluxing EG, *Cryst. Growth Des.* 9 (2009) 991–996.

[35] S.-P. Hu, C.-Y. Xu, W.-S. Wang, F.-X. Ma, L. Zhen, Synthesis of Bi₂WO₆ hierarchical structures constructed by porous nanoplates and their associated photocatalytic properties under visible light irradiation, *Ceram. Int.* 40 (2014) 11689–11698.

[36] L. Liang, Y. Tursun, A. Nulahong, T. Dilinuer, A. Tunishaguli, G. Gao, A. Abulikemu, K. Okitsu, Preparation and sonophotocatalytic performance of hierarchical Bi₂WO₆ structures and effects of various factors on the rate of Rhodamine B degradation, *Ultrasound. Sonochem.* 39 (2017) 93–100.

[37] M. Mishra, D.-M. Chun, α-Fe₂O₃ as a photocatalytic material: a review, *Appl. Catal. A Gen.* 498 (2015) 126–141.

[38] X. Liu, Q. Lu, C. Zhu, S. Liu, Enhanced photocatalytic activity of α-Fe₂O₃/Bi₂WO₆ heterostructured nanofibers prepared by electrospinning technique, *RSC Adv.* 5 (2015) 4077–4082.

[39] C. Jaramillo-Páez, J.A. Navío, M.C. Hidalgo, A. Bouziani, M.E. Azzouzi, Mixed α-Fe₂O₃/Bi₂WO₆ oxides for photoassisted hetero-Fenton degradation of methyl orange and phenol, *J. Photochem. Photobiol. A: Chem.* 332 (2017) 521–533.

[40] R. Chen, J. Lu, J. Xiao, C. Zhu, S. Peng, T. Chen, α-Fe₂O₃ supported Bi₂WO₆ for photocatalytic degradation of gaseous benzene, *Solid State Sci.* 71 (2017) 14–21.

[41] J. Zhang, L. Huang, H. Jin, Y. Sun, X. Ma, E. Zhang, H. Wang, Z. Kong, J. Xi, Z. Ji, Constructing two-dimension Mo₂S₃/Bi₂WO₆ core–shell heterostructure as carriers transfer channel for enhancing photocatalytic activity, *Mater. Res. Bull.* 85 (2017) 140–146.

[42] Y. Chen, J. Fang, S. Lu, W. Xu, Z. Liu, X. Xu, Z. Fang, One-step hydrothermal synthesis of BiOI/Bi₂WO₆ hierarchical heterostructure with highly photocatalytic activity, *J. Chem. Technol. Biotechnol.* 90 (2014) 947–954.

[43] Y. Tian, B. Chang, J. Lu, J. Fu, F. Xi, X. Dong, Hydrothermal synthesis of graphitic carbon nitride–Bi₂WO₆ heterojunctions with enhanced visible light photocatalytic activities, *ACS Appl. Mater. Interfaces* 5 (2013) 7079–7085.

[44] Y. Liao, H. Zhang, Z. Zhong, L. Jia, F. Bai, J. Li, P. Zhong, H. Chen, J. Zhang, Enhanced visible-photocatalytic activity of anodic TiO₂ nanotubes film via decoration with CuInSe₂ nanocrystals, *ACS Appl. Mater. Interfaces* 5 (2013) 11022–11028.

[45] C. Pan, J. Xu, Y. Wang, D. Li, Y. Zhu, Dramatic activity of C₃N₄/BiPO₄ photocatalyst with core/shell structure formed by self-assembly, *Adv. Funct. Mater.* 22 (2012) 1518–1524.

[46] Q.-H. Ren, Y. Zhang, H.-L. Lu, Y.-P. Wang, W.-J. Liu, X.-M. Ji, A. Devi, A.-Q. Jiang, D.W. Zhang, Atomic layer deposition of nickel on ZnO nanowire arrays for high-performance supercapacitors, *ACS Appl. Mater. Interfaces* 10 (2018) 468–476.

[47] W. Xiong, Q. Guo, Z. Guo, H. Li, R. Zhao, Q. Chen, Z. Liu, X. Wang, Atomic layer deposition of nickel carbide for supercapacitors and electrocatalytic hydrogen evolution, *J. Mater. Chem. A* 6 (2018) 4297–4304.

[48] M. Nasilowski, L. Nienhaus, S.N. Bertram, M.G. Bawendi, Colloidal atomic layer deposition growth of PbS/CdS core/shell quantum dots, *Chem. Commun.* 53 (2017) 869–872.

[49] S. Selvaraj, H. Moon, J.-Y. Yun, D.-H. Kim, Iron oxide grown by low-temperature atomic layer deposition, *Korean J. Chem. Eng.* 33 (2016) 3516–3522.

[50] M. Zafar, J.-Y. Yun, D.-H. Kim, Performance of inverted organic photovoltaic cells with nitrogen doped TiO₂ films by atomic layer deposition, *Korean J. Chem. Eng.* 35 (2018) 567–573.

[51] R. Tang, H. Su, Y. Sun, X. Zhang, L. Li, C. Liu, B. Wang, S. Zeng, D. Sun, Facile Fabrication of Bi₂WO₆/Ag₂S Heterostructure with Enhanced Visible-Light-Driven Photocatalytic Performances, *Nanoscale Res. Lett.* 11 (2016) 126.

[52] Z.W. Ai, Y. Wu, H. Wu, T. Wang, C. Chen, Y. Xu, C. Liu, Enhanced band-edge photoluminescence from ZnO-passivated ZnO nanoflowers by atomic layer deposition, *Nanoscale Res. Lett.* 8 (2013) 105.

[53] A. Ghobadi, T.G. Ulusoy, R. Garifullin, M.O. Guler, A.K. Okyay, A heterojunction design of single layer hole tunneling ZnO passivation wrapping around TiO₂ nanowires for superior photocatalytic performance, *Sci. Rep.* 6 (2016) 30587.

[54] Y. Hu, F. Li, D. Han, T. Wu, Q. Zhang, L. Niu, Y. Bao, Simple and label-free electrochemical assay for signal-on DNA hybridization directly at undecorated graphene oxide, *Anal. Chim. Acta* 753 (2012) 82–89.

[55] Z. Zhang, P. Wang, Optimization of photoelectrochemical water splitting performance on hierarchical TiO₂ nanotube arrays, *Energy Environ. Sci.* 5 (2012) 6506–6512.

[56] H. Wu, Z. Zheng, Y. Tang, N.M. Huang, R. Amal, H.N. Lim, Y.H. Ng, Pulsed electrodeposition of CdS on ZnO nanorods for highly sensitive photoelectrochemical sensing of copper (II) ions, *Sustain. Mater. Technol.* 18 (2018) e00075.

[57] J. Qian, Z. Yang, C. Wang, K. Wang, Q. Liu, D. Jiang, Y. Yan, K. Wang, One-pot synthesis of BiPO₄ functionalized reduced graphene oxide with enhanced photoelectrochemical performance for selective and sensitive detection of chlorpyrifos, *J. Mater. Chem. A* 3 (2015) 13671–13678.

[58] D. Jiang, X. Du, D. Chen, Y. Li, N. Hao, J. Qian, H. Zhong, T. You, K. Wang, Facile wet chemical method for fabricating p-type BiOBr/n-type nitrogen doped graphene composites: Efficient visible-excited charge separation, and high-performance photoelectrochemical sensing, *Carbon* 102 (2016) 10–17.

[59] R. Shukla, G. Madras, Cyclic reaction network modeling for the kinetics of photoelectrocatalytic degradation, *J. Environ. Chem. Eng.* 2 (2014) 780–787.

[60] Y. Zhou, M. Zhang, J. Lin, Z. Long, H. Zhang, J. Lin, C.-S. Wu, X. Wang, Monolayered Bi₂WO₆ nanosheets mimicking heterojunction interface with open surfaces for photocatalysis, *Nat. Commun.* 8340 (2015) 1–6.

[61] L. Wu, J. Bi, Z. Li, X. Wang, X. Fu, Rapid preparation of Bi₂WO₆ photocatalyst with nanosheet morphology via microwave-assisted solvothermal synthesis, *Catal. Today* 131 (2008) 15–20.

[62] T. Zhou, J. Hu, J. Li, Er³⁺ doped bismuth molybdate nanosheets with exposed {010} facets and enhanced photocatalytic performance, *Appl. Catal. B* 110 (2011) 221–230.

[63] Y. Zhang, L. Xiao, K. Xu, J. Song, F. Zhao, Graphene oxide-enveloped Bi₂WO₆ composites as a highly efficient catalyst for the thermal decomposition of cyclo-trimethylenetrinitramine, *RSC Adv.* 6 (2016) 42428–42434.

[64] J.A. Ramos Guijar, E.A. Sánchez, F. Bruns, E. Sadrollahi, M.A. Morales, E.O. López, F.J. Litterst, Vacancy ordered γ-Fe₂O₃ nanoparticles functionalized with nanohydroxyapatite: XRD, FTIR, TEM, XPS and Mössbauer studies, *Appl. Surf. Sci.* 389 (2016) 721–734.

[65] F. Kraushofer, Z. Jakub, M. Bichler, J. Hulva, P. Drmota, M. Weinold, M. Schmid, M. Setvin, U. Diebold, P. Blaha, G. Parkinson, Atomic-scale structure of the hematite α-Fe₂O₃ (1 102) “R-Cut” surface, *J. Phys. Chem. C* 122 (2018) 1657–1669.

[66] V. Kumar, F. Singh, O. Ntwaeborwa, H. Swart, Effect of Br⁻⁶ ions on the structural, morphological and luminescent properties of ZnO/Si thin films, *Appl. Surf. Sci.* 279 (2013) 472–478.

[67] Y. Cong, Y. Ji, Y. Ge, H. Jin, Y. Zhang, Q. Wang, Fabrication of 3D Bi₂O₃-BiOI

heterojunction by a simple dipping method: highly enhanced visible-light photocatalytic activity, *Chem. Eng. J.* 307 (2017) 572–582.

[68] C. Li, S. Yu, H. Dong, C. Liu, H. Wu, H. Che, G. Chen, Z-scheme mesoporous photocatalyst constructed by modification of Sn₃O₄ nanoclusters on g-C₃N₄ nanosheets with improved photocatalytic performance and mechanism insight, *Appl. Catal. B Environ.* 238 (2018) 284–293.

[69] C. Li, S. Yu, H. Dong, Y. Wang, H. Wu, X. Zhang, G. Chen, C. Liu, Mesoporous ferriferrous oxide nanoreactors modified on graphitic carbon nitride towards improvement of physical, photoelectrochemical properties and photocatalytic performance, *J. Colloid Interface Sci.* 531 (2018) 331–342.

[70] H. Che, G. Che, E. Jiang, C. Liu, H. Dong, C. Li, A novel Z-Scheme CdS/Bi₃O₄Cl heterostructure for photocatalytic degradation of antibiotics: mineralization activity, degradation pathways and mechanism insight, *J. Taiwan Inst. Chem. Eng.* 91 (2018) 224–234.

[71] C. Li, G. Chen, J. Sun, Y. Feng, J. Liu, H. Dong, Ultrathin nanoflakes constructed erythrocyte-like Bi₂W₆O₆ hierarchical architecture via anionic self-regulation strategy for improving photocatalytic activity and gas-sensing property, *Appl. Catal. B Environ.* 163 (2015) 415–423.

[72] C. Li, G. Chen, J. Sun, J. Rao, Z. Han, Y. Hu, W. Xing, C. Zhang, Doping effect of phosphate in Bi₂WO₆ and universal improved photocatalytic activity for removing various pollutants in water, *Appl. Catal. B Environ.* 188 (2016) 39–47.